Opto-Electronic Advances

CN 51-1781/TN ISSN (Print) 2096-4579 ISSN (Online) 2097-3993

# Ultrahigh-efficiency and robust thermophotovoltaic devices via spectral-heat filtering

Heng Zhang, Zhequn Huang, Min Ding, Yilin Feng, Jian Zhang, Tao Deng, Hongxing Xu and Kehang Cui*

**Citation:** Zhang H, Huang ZQ, Ding M et al. Ultrahigh-efficiency and robust thermophotovoltaic devices via spectral-heat filtering. *Opto-Electron Adv* **9**, 250248 (2026).

https://doi.org/10.29026/oea.2026.250248

Received: 17 September 2025; Accepted: 7 April 2026; Published online: 27 May 2026

## Related articles

Ultrahigh performance passive radiative cooling by hybrid polar dielectric metasurface thermal emitters

Yinan Zhang, Yinggang Chen, Tong Wang, et al

*Opto-Electronic Advances* 2024, **7**(4): 230194 doi: 10.29026/oea.2024.230194

Single-beam optical trap-based surface-enhanced Raman scattering optofluidic molecular fingerprint spectroscopy detection system

Ning Sun, Yuan Gan, Yujie Wu, et al

*Opto-Electronic Advances* 2025, **8**(2): 240182 doi: 10.29026/oea.2025.240182

**More related articles in Opto-Electronic Journals Group website**

Opto-Electronic Journals Group

https://www.oejournal.org

OE_Journal

@OptoElectronAdv

OEA | Opto-Electronic Advances

Article

September 2026, Vol. 9, No. 9

Open Access

# Ultrahigh-efficiency and robust thermophotovoltaic devices via spectral-heat filtering

Heng Zhang[1], Zhequn Huang[2], Min Ding[3], Yilin Feng[1], Jian Zhang[4], Tao Deng[1], Hongxing Xu[5] and Kehang Cui[1]*

**Abstract:** Thermophotovoltaics (TPVs) are solid-state photonic heat engines that convert thermal radiation into continuous power generation through photovoltaics. Recent work on photon recuperation using back-surface reflectors has remarkably boosted TPV efficiencies. However, building a practical TPV device with photons actually recuperated remains a challenge because of the strong emitter-cell thermal coupling. Here we build a robust TPV device through emitter-side photon recuperation using a spectral-heat filter (SHF). The SHF, optimized via multi-objective machine learning, blocks 99% of the sub-bandgap radiation as well as the thermal conduction and convection from the emitter. The accelerated thermal ageing test shows the fabricated SHF has a L70-rated lifetime of 57,477 hours. The emitter-SHF pair decouples the temperature-susceptible PV cell from the photon-recuperation process, and unlocks the mass-produced state-of-the-art photovoltaic cells for use in TPV. The emitter-SHF pair engineers the above-bandgap radiation to achieve current matching in the GaInP/GaAs/Ge triple-junction photovoltaic cell. The efficiency of the TPV device reaches 47.16% ± 1.12% at the emitter temperature of 2,162 °C. The spectral-heat filtering architecture offers inherent operational robustness as well as the power conversion efficiency surpassing conventional heat engines.

**Keywords:** spectral control; photonic heat engine; thermophotovoltaics; machine learning

DOI: 10.29026/oea.2026.250248 | CSTR: 32247.14.oea.2026.250248

**Citation:** Zhang H, Huang ZQ, Ding M et al. Ultrahigh-efficiency and robust thermophotovoltaic devices via spectral-heat filtering. *Opto-Electron Adv* **9**, 250248 (2026).

## 1 Introduction

Thermophotovoltaics (TPVs) are radiative heat engines that convert the above-bandgap ($E \geq E_g$) radiation from a thermal emitter operating at above 1000 °C to electricity through a photovoltaic (PV) cell[1–8]. Other heat transfer pathways of the emitter-cell pair, including sub-bandgap ($E < E_g$) radiation and non-radiative heat transfer (conduction and convection), do not contribute to the power output and may cause temperature rise which is detrimental to TPV devices. Spectral (radiative) and thermal (non-radiative) management is the key to realize high power conversion efficiencies of TPVs. Extensive efforts have been invested in spectral management, such as recuperating the $E < E_g$ photons using front-surface filter[9–12] and back-surface reflectors (BSRs)[1–5,13,14], or suppressing the $E < E_g$ photons using spectral-selective emitters[15–21]. Recent breakthrough on $E < E_g$ photon recuperation using BSRs has boosted the radiative heat conversion efficiency to *ca.* 44%[5]. However, to actually recuperate the $E < E_g$ photons, the emitter and the PV cell should be closely placed and thus thermally coupled (Fig. 1(a)). Taking non-radiative heat transfer into consideration would degrade the TPV device efficiency and service reliability[6].

Placing an optical filter near the emitter could block the non-radiative heat transfer and decouple the temperature-sensitive PV cell from the photon recuperating process, thus could be a promising pathway for simultaneous spectral and thermal management[10,22,23]. Nevertheless, achieving near-unity reflectance over the entire sub-bandgap wavelength range for the optical filter remains a challenge. Conventional optical structures[24] such as quarter-wave stacks,

Received: 17 September 2025

Accepted: 7 April 2026

Published online: 27 May 2026

[1]School of Material Science and Engineering, State Key Laboratory of Metal Matrix Composites, Center for Hydrogen Science, Shanghai Jiao Tong University, Shanghai 200240, China; [2]Zhiyuan Innovative Research Center, Shanghai Jiao Tong University, Shanghai 200240, China; [3]Shanghai HeiYi Materials Technology Co. Ltd., Shanghai 200240, China; [4]Research Center for Transparent Ceramics, Shanghai Institute of Ceramics, Chinese Academy of Sciences, Shanghai 200050, China; [5]Wuhan Institute of Quantum Technology, Wuhan University, Wuhan 430072, China.
*Correspondence: KH Cui, E-mail: cuikehang@sjtu.edu.cn

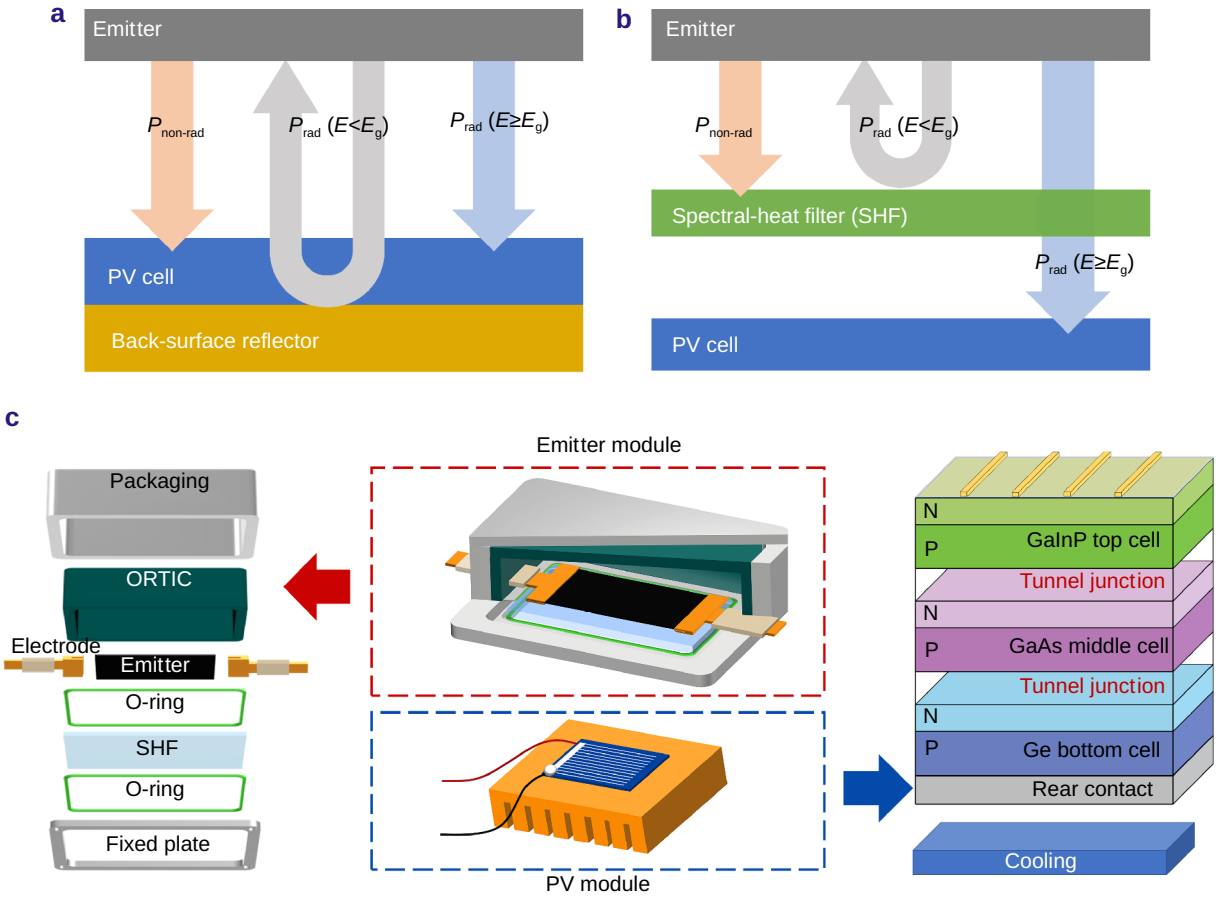


Fig. 1 | Device architecture and photon management. (a) Energy balance and flow of the BSR-TPV system. The thermal component (blackbody emitter) and the electronic component (PV cell) are thermally coupled. $P_{rad}(E < E_g)$, $P_{rad}(E \geq E_g)$, and $P_{non\text{-}rad}$ denote the power of the sub-bandgap radiation, the power of the above-bandgap radiation, as well as the power of the combined thermal conduction and convection, respectively. (b) Energy balance and flow of the SHF-TPV system. The SHF blocks $P_{rad}(E < E_g)$ and $P_{non\text{-}rad}$, and engineers $P_{rad}(E \geq E_g)$. The thermal component (blackbody emitter) and the electronic component (PV cell) are thermally decoupled. (c) Device architecture of the SHF-TPV system which consists of the emitter module and the PV module. The PV module is mounted on a thermally conductive heat sink and passively cooled without additional energy consumption.

chirped mirrors and distributed Bragg reflectors have relative narrow reflection bandwidths and suffer from group delay dispersion oscillations. Superimposing multiple filters, such as rugate stack[25–27], could broaden the reflection bandwidth. However, this will require hundreds of layers with millimeter-scale thickness, resulting in accumulation of non-stoichiometric impurities and severe absorption losses. The TPV device based on a near-emitter filter has not been experimentally realized yet.

Here we realize a sub-μm-thick, ultra-broadband, omnidirectional spectral-heat filter (SHF) and build a scalable, robust and efficient TPV device based thereupon. Our device is architected as follows (Fig. 1(b) and 1(c)). The carbon-nanotube emitter (CNE) with near blackbody emittance and high thermal stability is placed inside a stainless-steel chamber with the inner wall covered with optical-reflective thermal-insulative ceramics (ORTIC). The SHF functions as a wavelength-selective radiation filter, effectively suppressing parasitic long-wavelength thermal emission while preserving useful photon flux for photovoltaic conversion, thereby improving overall energy utilization efficiency. The SHF blocks thermal conduction, convection and $E < E_g$ thermal radiation from the CNE, and thermally separates the TPV device into the hot region (the emitter module) and the cool region (the PV module). The $E < E_g$ photon-recuperation process is accomplished within the emitter module through the CNE-SHF pair. The CNE-SHF pair also engineers the $E \geq E_g$ radiation to match the band structures of the PV cell. The temperature-susceptible PV cell is taken out of the emitter module, hence is inherently robust and reliable. The modularity design provides flexibility in device configuration and unlocks the state-of-the-art PV cells for use in TPV. Here we adopt the GaInP/GaAs/Ge triple-junction photovoltaic (3JPV) cell which is the standard PV cell used in spacecrafts (Fig. 1(c)). This is for two reasons. The low-bandgap sub-cell helps

mitigate the efficiency penalty associated with the finite spectral transition region near the band edge. In practical TPV systems, neither the emitter spectrum nor the optical filter exhibits an ideal step-function cutoff at $E = E_g$. Instead, there exists a finite energy interval around the bandgap where photons with $E < E_g$ may partially transmit to the PV cell but cannot generate photocurrent, while photons with $E \geq E_g$ may be partially suppressed or not fully absorbed due to the gradual onset of semiconductor absorption. This unavoidable non-ideal spectral transition leads to parasitic heat transfer and incomplete photon utilization. By extending the absorption range to lower photon energies, the Ge bottom sub-cell reduces the fraction of photons residing in this transition region, thereby alleviating the associated efficiency loss. Moreover, the 3JPV is mass-produced with industry manufacturing infrastructure, paving the way for scalable deployment of the TPV devices.

## 2 Results and discussion

### 2.1 Spectral-heat filter

We design the SHF using a machine-learning multi-objective optimization (MOO) framework (see Supplementary Section 2). The optimization objectives of the MOO framework are set as follows. i) $obj_{\text{spectral}}$ evaluates the average deviation between the designed transmittance and the ideal transmittance. $obj_{\text{spectral}}$ is the figure of merit for the spectral selectivity, and is critical to the efficiency of the TPV device. ii) $obj_{\text{heat}}$ evaluates the optical absorption loss in the entire wavelength range. $obj_{\text{heat}}$ is critical to the service reliability of the device, as the optical absorption loss would result in the temperature rise of the SHF. The optimal structure is obtained by screening the Pareto optimal front of the evolving generations. After 80 generations of iterations, the deviation between the ideal and the designed objectives is less than 5% (Fig. 2(a)). Considering the manufacturability, the selected SHF consists of 9 layers (24.9 nm $HfO_2$, 7.9 nm Ag-Ge alloy, 119.6 nm $SiO_2$, 6.6 nm $HfO_2$, 9.5 nm Ag-Ge alloy, 135.1 nm $SiO_2$, 3.6 nm $Al_2O_3$, 55.2 nm $HfO_2$ and 55.5 nm $Al_2O_3$) with a total thickness of 417.9 nm (Supplementary Fig. S1). The electromagnetic field distribution of the designed SHF (Fig. 2(b) and Supplementary Fig. S2) shows a strong field suppression in the sub-bandgap wavelength range, and no field enhancement or suppression in the above-bandgap wavelength range. Using $HfO_2$, a high-index dielectric, suppresses the excitation of surface plasmons at the Ag interface within the operating spectral range, which reduces the absorption loss and enables high transmission of the overall structure.

We fabricate the SHF on a 3-mm-thick fused quartz substrate using atomic layer deposition and electron beam evaporation (see Supplementary Section 1). The fabricated SHF is uniform and visually transparent (Fig. 2(c)). Under the infrared thermal camera (Fig. 2(d)), the fabricated SHF shows a very low thermal emissivity and effectively blocks the ambient radiation in the mid- and far-infrared range, demonstrating infrared stealth characteristics. The spectral properties of the fabricated SHF were characterized in the wavelength range of 0.25–16.67 μm using UV-Vis-NIR spectrophotometer and Fourier-transform infrared (FT-IR) spectroscopy with integration sphere accessories (see Fig. 2(e–f) and Supplementary Figs. S3–S5). The angle-resolved UV-Vis-NIR spectroscopy (Fig. 2(e), Supplementary Fig. S5) results show that the spectral properties of the SHF are angular-independent, which is important to harvest thermal emission from all incident angles. Within the SHF structure, the double silver layer and intermediate dielectric layer collectively form a Fabry-Pérot (F-P) resonator. Given the refractive index and thickness of the intermediate dielectric layer, the angular sensitivity of the resonance is extremely low. As weighted by 2,162 °C blackbody radiation spectrum, the average reflectance, transmittance and absorbance in the entire sub-bandgap wavelength range 1.80–16.67 μm are 0.929, 0.011 and 0.060, respectively.

The surface topography mapping by atomic force microscopy (AFM) shows that the RMS roughness of the fabricated SHF is 2.347 nm (Supplementary Fig. S6). The smooth surface is beneficial to suppress the optical absorption loss related with scattering and the localized surface plasmon resonance (LSPR). We characterize the uniformity of the fabricated SHF over a large area (25 mm × 50 mm) using spectroscopic ellipsometry mapping (see Experimental Section). The variations of the ellipsometry parameters Δ (Fig. 2(g)) and Ψ (Fig. 2(h)) at the 75 test locations (marked in Supplementary Fig. S7) throughout the entire sample are negligible, indicating the uniformity in both the structure and the optical property of the fabricated SHF.

### 2.2 Thermophotovoltaic device

We build the emitter module by suspending the CNE near the fabricated SHF inside a stainless-steel chamber with the inner wall covered with optical-reflective thermal-insulative ceramics (see Supplementary Fig. S8). The chamber is filled with argon to provide an inert atmosphere. The SHF serves as the window of photon and heat flow management for the emitter module. During operation, the highest temperature achieved by the CNE through Joule heating is 2,162 °C. The SHF is also heated up by optical absorption and the conductive/convective heat transfer. We record the temperature rise of the SHF. At the operating temperature of 2,162 °C, the temperature of the SHF stabilizes at 114.8 °C without intentional cooling (Fig. 3(a)). We examine the in-situ spectral performance of the emitter module using a fiber-optic CCD-array spectrometer. The spectrum (the red line in Fig. 3(b)) matches well with the weighted transmittance (2,162 °C blackbody radiation) measured by UV-Vis-NIR spectrophotometer (the green line in Fig. 3(b)).

To examine the service reliability of the fabricated SHF,

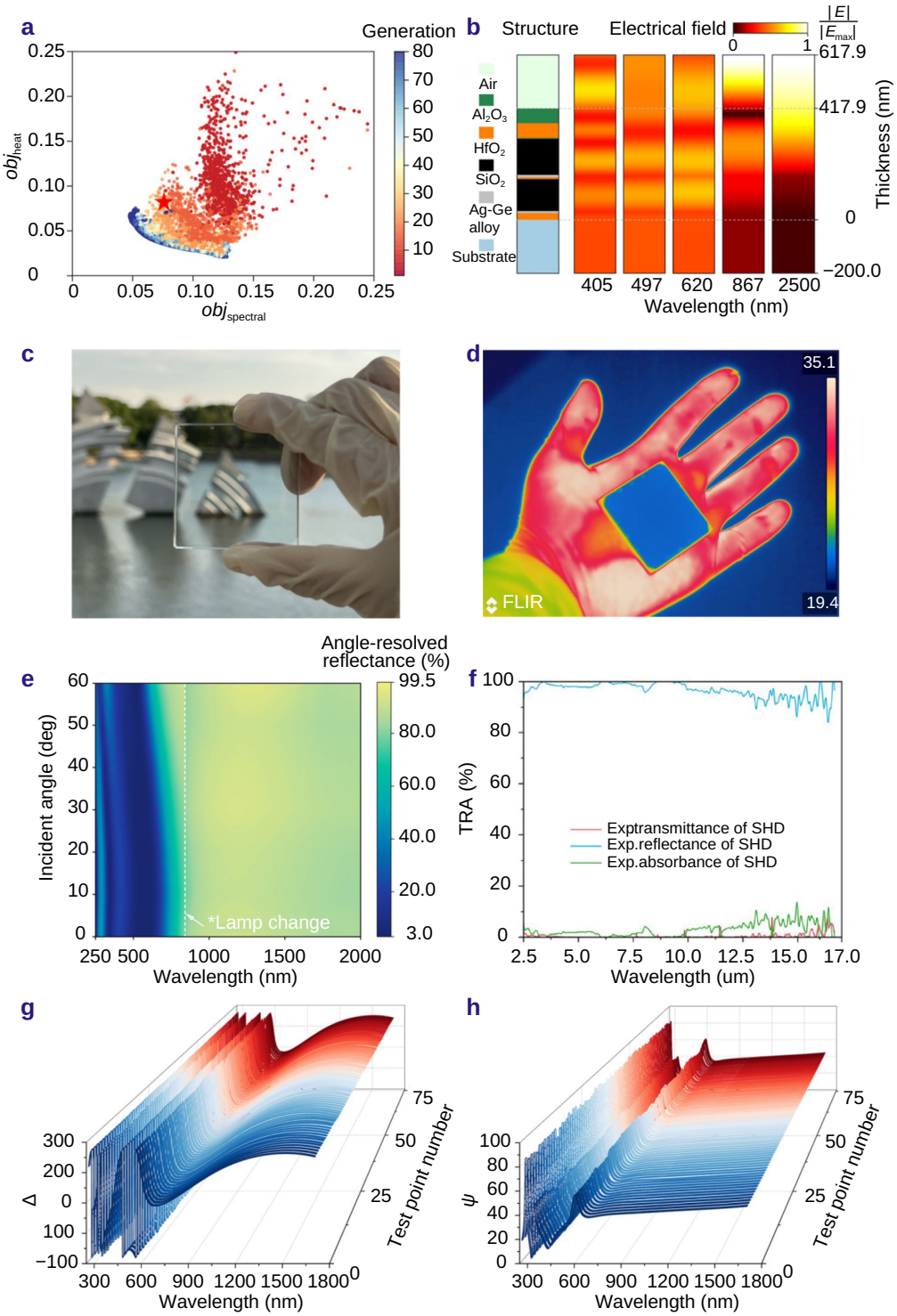


Fig. 2 | Design and fabrication of the SHF. (a) Evolution of the Pareto front of $obj_{spectral}$ and $obj_{heat}$ in the multi-objective machine-learning optimization (MMO) framework. The red star marks the selected SHF design. (b) Electric field distribution of the optimized SHF at the wavelengths of 405 nm, 497 nm, 620 nm, 867 nm and 2500 nm. The top and bottom gray dashed lines mark the SHF/air interface and the SHF/quartz substrate interface, respectively. Full-spectrum electromagnetic field distribution of the selected SHF is given in Supplementary Fig. S2. (c) Optical photograph of the fabricated SHF (50 mm × 50 mm). (d) Infrared thermal imaging of the fabricated SHF. (e) Experimental angle-resolved reflectance of the fabricated SHF from 0° to 60°. (f) Experimental infrared hemispherical transmittance, reflectance and absorbance of the fabricated SHF at the wavelength range of 2.5–16.67 μm. (g, h) Spectral ellipsometry results Δ (g) and Ψ (h) at 75 test points on the fabricated SHF. The positions of the 75 test points are given in Supplementary Fig. S7.

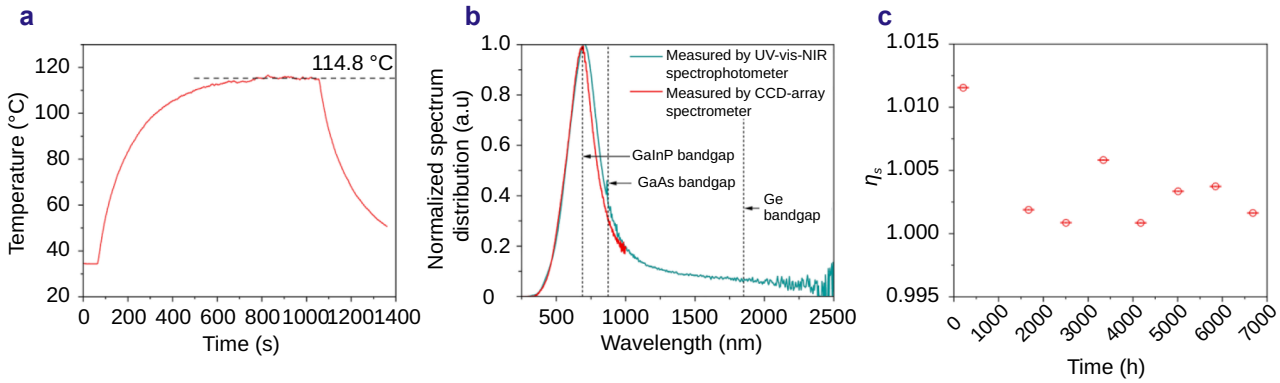


Fig. 3 | Performance of the SHF at high temperature. (a) The SHF temperature as the function of time at the emitter temperature of 2,162 °C. (b) Normalized spectral distribution at the emitter temperature of 2,162 °C. The red line denotes the experimental data measured by a fiber-optic CCD-array spectrometer, and the green line denotes the 2,162 °C blackbody radiation-weighted transmittance measured by UV-Vis-NIR spectrophotometer. (c) The variation of the thermal stability FOM of the fabricated SHF throughout the accelerated thermal ageing test.

we carry out an accelerated thermal ageing test at 280 °C (see Supplementary Section 1). The thermal stability figure of merit (FOM) is defined as the ratio of the spectral efficiency before and after the accelerated ageing test after 384 hours (see Experimental Section). This ageing time corresponds to a reliable operation for 6,682 hours at the emitter temperature of 2,162 °C (Fig. 3(c)). After the accelerated ageing test, the variation of the FOM is negligible (the transmittance and reflectance spectra before and after the test are shown in Supplementary Fig. S9). Based on the L70 standard (see Supplementary Section 1), the lifetime of the fabricated SHF is estimated as 57,477 hours. The lifetime can be elongated to 84,234 hours by reducing the temperature of the SHF to 100 °C through effective cooling.

We build the TPV device by assembling the emitter module and the PV module. The GaInP/GaAs/Ge 3JPV cells (the GaInP top sub-cell with the bandgap of 1.71 eV and spectral response range of 334–727 nm, the GaAs middle sub-cell with the bandgap of 1.29 eV and spectral response range of 590–963 nm, the Ge bottom sub-cell with the bandgap of 0.69 eV and spectral response range of 860–1806 nm) fabricated on a 4-inch wafer (Fig. 4(a)) are cut into 10 mm × 10 mm pieces (Supplementary Figs. S10–S11). The PV module is placed close to the emitter module with the distance of 1 mm for near-unity view factor (see Supplementary Figs. S12–S13). During operation, the energy input to the emitter module results in the temperature rise of the CNE (2,162 °C) and the SHF (114.8 °C). The illumination of the emitter module, which appears a white color (Fig. 4(b)), is incident on the PV module and then converted to electricity. The power conversion efficiency (PCE) $\eta_{\mathrm{TPV}}$ is defined by the electrical power output generated by the PV module $P_{\mathrm{out}}$ over the heat transfer power of the emitter module $Q_{\mathrm{h}}$,

$$\eta_{\mathrm{TPV}} = \frac{P_{\mathrm{out}}}{Q_{\mathrm{h}}} = \frac{P_{\mathrm{out}}}{P_{\mathrm{emitter\text{-}PV}} + P_{\mathrm{filter\text{-}PV}}}, \quad (1)$$

where $P_{\mathrm{emitter\text{-}PV}}$ and $P_{\mathrm{filter\text{-}PV}}$ denote the heat transfer power from the CNE and the SHF of the emitter module to the PV module.

Under illumination of the emitter module, $P_{\mathrm{out}}$ is obtained from the current density-voltage ($J$-$V$) characteristics of the PV cell measured by a semiconductor analyzer. Both open circuit voltage ($V_{\mathrm{oc}}$) and short-circuit current density ($J_{\mathrm{sc}}$) increase with the increase of the emitter temperature (see Fig. 4(c)). Fill factor ($FF$) decreases slightly with the increase of the emitter temperature (see Fig. 4(d), Supplementary Fig. S14), owing to the increased Joule heating loss caused by the series resistance (0.2 Ω·cm²) and the increased current density. At the emitter temperature of 2,162 °C, $V_{\mathrm{oc}}$, $J_{\mathrm{sc}}$, $FF$ and $P_{\mathrm{out}}$ are 2707.10 ± 39.30 mV, 109.99 ± 2.04 mA/cm², 79.80% ± 0.20%, and 237.6 ± 5.6 mW/cm² (see Supplementary Section 1), respectively. A complete parametric set of the measured $J_{\mathrm{sc}}$, $V_{\mathrm{oc}}$, $FF$, $P_{\mathrm{out}}$ and $\eta_{\mathrm{TPV}}$ values is provided in Supplementary Table S5 and Supplementary Fig. S14. We note that the relatively low output power density compared with recent TPV demonstrations[1,4] is not caused by the spectral engineering of the SHF (shielding of the above-bandgap radiation). Implementing a filter with near-unity transmittance would enhance radiative power from 469.5 mW/cm² to 4.33 W/cm², yet the output power density would rise only marginally to 348.4 mW/cm². This limitation stems from the large bandgap (1.80 eV) of the top cell. In contrast, adopting a single-junction PV cell with a bandgap matching the bottom cell (0.67 eV) could drastically increase output power density to 2.35 W/cm² (see Supplementary Section 7), a value comparable to those in Tervo et al.[4] and LaPotin et al[1]. The performance combination demonstrated in our work serves as a proof-of-concept, validating the applicability of modular architecture for diverse TPV device designs in different scenarios.

The challenge of accurate characterization of $Q_{\mathrm{h}}$ lies in the ultrabroad spectral distribution of radiative power combining the CNE and the SHF as well as the non-radiative

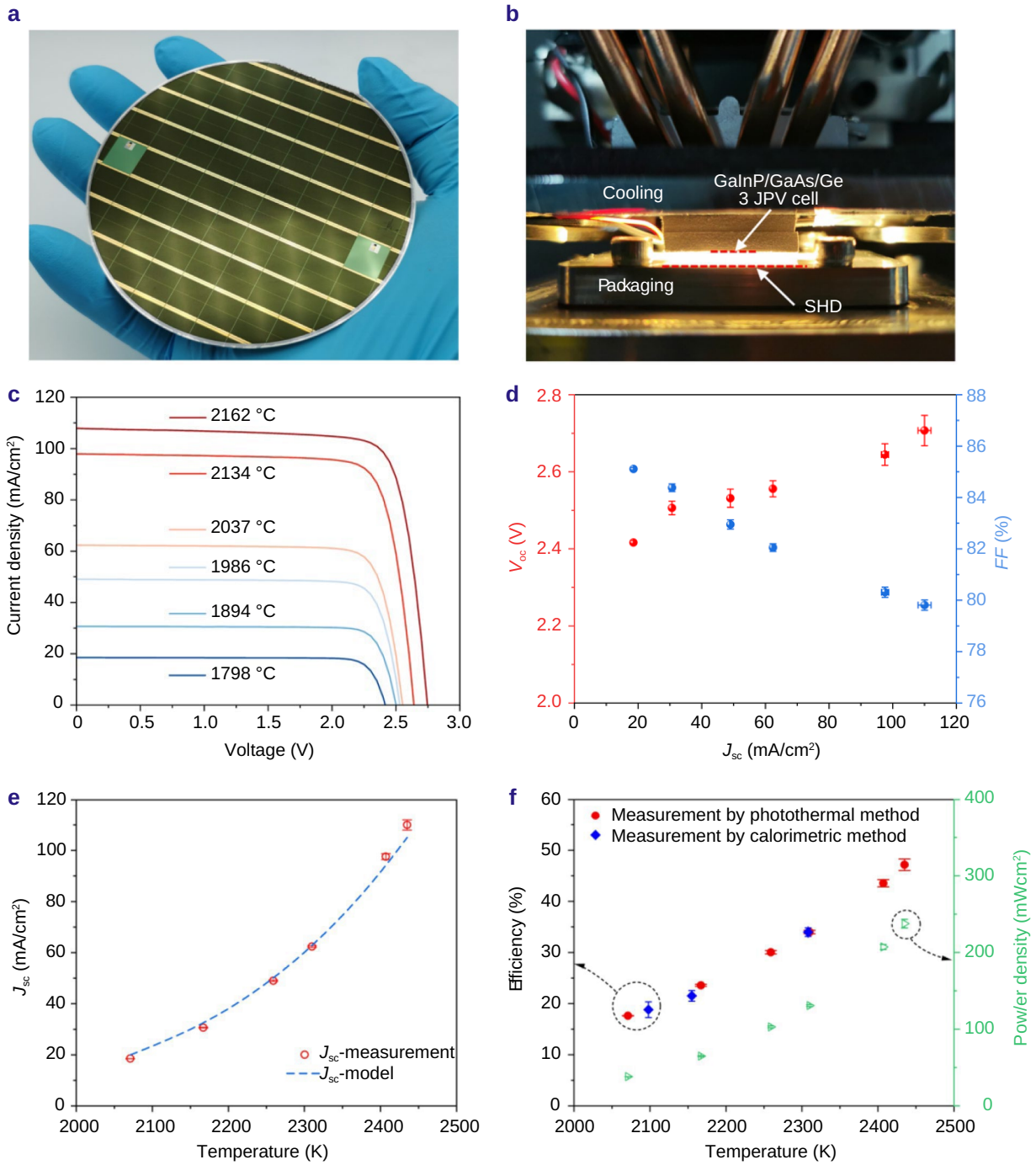


Fig. 4 | TPV device characterization. (a) Photograph of the 4-inch GaInP/GaAs/Ge 3JPV cell. (b) Photograph of the TPV device during operation. The distance between the GaInP/GaAs/Ge 3JPV cell and the SHF is 1 mm. (c) The *J-V* curves of the TPV device at different emitter temperatures. (d) $V_{oc}$ versus $J_{sc}$ (red dots) and *FF* versus $J_{sc}$ (blue dots) measurements under TPV operation. The corresponding results of $V_{oc}$, $J_{sc}$, *FF* and emitter temperature are shown in Supplementary Fig. S14. (e) The measured and modelled $J_{sc}$ at different emitter temperatures. (f) The TPV efficiency measured by the photothermal method and the calorimetric method and power density of TPV device at different emitter temperatures.

(conductive/convective) heat transfer involved in the SHF-PV pair (see thermodynamic analysis in Supplementary Section 3). We employ two methods, i.e., the photothermal method and the calorimetric method to characterize $Q_h$ for cross corroboration (see Supplementary Section 4). The calorimetric method utilizes a heat flux sensor (HFS) to measure total heat absorbed in the PV module $P_{HFS}$. The reflected radiative power by the PV module $P_{cell_refl}$ in our

device cannot be recuperated by the emitter. Thus, $Q_h$ characterized by the calorimetric method is the sum of $P_{out,}$ $P_{HFS}$ and $P_{cell_refl}$. The photothermal method utilizes a thermopile power sensor (TPS) to capture the incident radiative power in the wavelength range of 0.2–11 μm $P_{TPS}$ where the radiation power from the CNE is predominately distributed. The radiative power distributed outside photothermal working bandwidth (11–65 μm) $P_{TPS\text{-}corr}$ of the TPS as well as the non-radiative heat transfer $P_{non\text{-}rad}$ are obtained based on the temperature of the SHF. Thus, $Q_h$ characterized by the photothermal method is the sum of $P_{TPS}$, $P_{TPS\text{-}corr}$ and $P_{non\text{-}rad}$. Figure 4(e) shows that the model prediction of the $J_{sc}$ based on the TPS-measured radiative power and external quantum efficiency (see Supplementary Section 5) of the 3JPV matches well with the experimentally measured $J_{sc}$. The good agreement demonstrates the accuracy of the TPS measurement.

At the emitter temperature of 2,162 °C, the $\eta_{TPV}$ of the TPV device is measured as 47.16% ± 1.12% (Fig. 4(f)), which is cross-corroborated by the photothermal method and the calorimetric method (see uncertainty propagation in Supplementary Section 6). The high $\eta_{TPV}$ is attributed to the spectral engineering at two levels. At the optical level, the sub-bandgap photons are blocked by the SHF and recycled by the emitter (see Supplementary Fig. S15). At the optoelectronic level, the ratio of the spectral response of the GaInP, GaAs and Ge junction subcells is 1 ∶ 0.998 ∶ 0.997 (see Supplementary Section 8). The spectral distribution incident on the PV satisfies the current matching condition for the GaInP, GaAs and Ge junction subcells, and thus maximizes the PCE of the PV cell.

We note that the triple-junction architecture considered here serves as a performance-oriented model to evaluate the upper-bound efficiency enabled by combining multi-bandgap conversion with selective photonic design. Multi-junction photovoltaic devices are predominantly deployed in space applications, as their terrestrial use is constrained by current-matching sensitivity under weather-induced spectral variations. In contrast, the spectrally controlled emission in thermophotovoltaic systems mitigates such spectral fluctuations, enabling improved current matching across sub-cells and more stable operation. These considerations suggest that TPV architectures may provide a viable pathway to extend multi-junction photovoltaic technologies toward terrestrial applications through emitter–cell spectral co-design.

## 3 Conclusions

This study presents a robust thermophotovoltaic (TPV) device that utilizes a spectral-heat filter (SHF), optimized via machine learning, to block 99% of sub-bandgap radiation and thermally decouple the emitter and photovoltaic cell. The SHF-TPV device achieves an efficiency of 47.16% ± 1.12% at 2,162 °C, surpassing conventional heat engines and enabling the integration of mass-produced photovoltaic cells into high-performance TPV systems. Moreover, our work demonstrates a conceptual framework that combining machine learning-aided filter design and multi-junction solar cells can effectively harvest near-band-edge sub-bandgap (transition band) radiation loss caused by the unavoidable non-ideal cutoff of practical TPV emitters and filters. The transition-band radiation loss has long been a challenge degrading the TPV efficiency.

While the high emitter temperature (~2500 K) considered here is adopted to evaluate the upper-bound TPV performance, the underlying design principles remain applicable to lower-temperature systems through spectral scaling. For TPV with lower operating temperatures (<1500 K), the SHF can be implemented by replacing the Ag/Ge layer with a mid-infrared plasmonic reflector such as highly doped semiconductors (e.g., Si, InAs, InGaAs) or transparent conducting oxides (e.g., ITO, AZO). The plasma frequency can be tuned via carrier concentration (typically $10^{19}$–$10^{21}$ $cm^{-3}$) to achieve strong reflection in the mid- to far-infrared.

Building on this framework, the TPV system could be further optimized by integrated spectral and bandgap engineering to simultaneous improve conversion efficiency and output power density in future multijunction TPV architectures. The high efficiency, modular design architecture and service reliability of the SHF-TPV device may open up new possibilities for wide-range applications, such as TW/TWh-scale thermal batteries[7,8,28,29], electric propulsion for interstellar rockets[30,31] and vehicles[32], etc.

## References

1. LaPotin A, Schulte KL, Steiner MA et al. Thermophotovoltaic efficiency of 40%. *Nature* **604**, 287–291 (2022).
2. Fan DJ, Burger T, McSherry S et al. Near-perfect photon utilization in an air-bridge thermophotovoltaic cell. *Nature* **586**, 237–241 (2020).
3. Omair Z, Scranton G, Pazos-Outón LM et al. Ultraefficient thermophotovoltaic power conversion by band-edge spectral filtering. *Proc Natl Acad Sci USA* **116**, 15356–15361 (2019).
4. Tervo EJ, France RM, Friedman DJ et al. Efficient and scalable GaInAs thermophotovoltaic devices. *Joule* **6**, 2566–2584 (2022).
5. Roy-Layinde B, Lim J, Arneson C et al. High-efficiency air-bridge thermophotovoltaic cells. *Joule* **8**, 2135–2145 (2024).
6. López E, Artacho I, Datas A. Thermophotovoltaic conversion efficiency measurement at high view factors. *Sol Energy Mater Sol Cells* **250**, 112069 (2023).
7. Amy C, Seyf HR, Steiner MA et al. Thermal energy grid storage using multi-junction photovoltaics. *Energy Environ Sci* **12**, 334–343 (2019).
8. Burger T, Sempere C, Roy-Layinde B et al. Present efficiencies and future opportunities in thermophotovoltaics. *Joule* **4**, 1660–1680 (2020).
9. Wernsman B, Siergiej RR, Link SD et al. Greater than 20% radiant heat conversion efficiency of a thermophotovoltaic radiator/module system using reflective spectral control. *IEEE Trans Electron Devices* **51**, 512–515 (2004).
10. Fourspring PM, DePoy DM, Rahmlow TD Jr et al. Optical coatings for thermophotovoltaic spectral control. *Appl Opt* **45**, 1356–1358

(2006).
11. Shemelya C, DeMeo DF, Vandervelde TE. Two dimensional metallic photonic crystals for light trapping and anti-reflective coatings in thermophotovoltaic applications. *Appl Phys Lett* **104**, 021115 (2014).
12. Zhang H, Huang ZQ, Ding M et al. A photon-recycling incandescent lighting device. *Sci Adv* **9**, eadf3737 (2023).
13. Tong JK, Hsu WC, Huang Y et al. Thin-film 'thermal well' emitters and absorbers for high-efficiency thermophotovoltaics. *Sci Rep* **5**, 10661 (2015).
14. Lee B, Lentz R, Burger T et al. Air-bridge Si thermophotovoltaic cell with high photon utilization. *ACS Energy Lett* **7**, 2388–2392 (2022).
15. Dyachenko PN, Molesky S, Petrov AY et al. Controlling thermal emission with refractory epsilon-near-zero metamaterials via topological transitions. *Nat Commun* **7**, 11809 (2016).
16. Arpin KA, Losego MD, Cloud AN et al. Three-dimensional self-assembled photonic crystals with high temperature stability for thermal emission modification. *Nat Commun* **4**, 2630 (2013).
17. Wang QX, Huang ZQ, Li JZ et al. Module-Level polaritonic thermophotovoltaic emitters via hierarchical sequential learning. *Nano Lett* **23**, 1144–1151 (2023).
18. Minsu O, McElearney J, Lemire A et al. Material candidates for thermally robust applications of selective thermophotovoltaic emitters. *Phys Rev Mater* **6**, 110201 (2022).
19. Dias MRS, Gong T, Duncan MA et al. Photonics roadmap for ultra-high-temperature thermophotovoltaics. *Joule* **7**, 2209–2227 (2023).
20. Woolf DN, Kadlec EA, Bethke D et al. High-efficiency thermophotovoltaic energy conversion enabled by a metamaterial selective emitter. *Optica* **5**, 213–218 (2018).
21. Kim Y, Kim MJ, Kim YS et al. Nanostructured radiation emitters: design rules for high-performance thermophotovoltaic systems. *ACS Photonics* **6**, 2260–2267 (2019).
22. McSherry S, Webb M, Kaufman J et al. Nanophotonic control of thermal emission under extreme temperatures in air. *Nat Nanotechnol* **17**, 1104–1110 (2022).
23. Ilic O, Bermel P, Chen G et al. Tailoring high-temperature radiation and the resurrection of the incandescent source. *Nat Nanotechnol* **11**, 320–324 (2016).
24. Razskazovskaya O, Krausz F, Pervak V. Multilayer coatings for femto- and attosecond technology. *Optica* **4**, 129–138 (2017).
25. De Luca D, Kortge D, Di Gennaro E et al. Ultra-thin sputter-deposited infrared rugate mirror for enhancing solar-to-thermal energy conversion. *Opt Lett* **47**, 230–233 (2022).
26. Bierman DM, Lenert A, Chan WR et al. Enhanced photovoltaic energy conversion using thermally based spectral shaping. *Nat Energy* **1**, 16068 (2016).
27. Ortabasi U, Bovard B. Rugate technology for thermophotovoltaic (TPV) applications: a new approach to near perfect filter performance. *AIP Conf Proc* **653**, 249–258 (2003).
28. Datas A, López-Ceballos A, López E et al. Latent heat thermophotovoltaic batteries. *Joule* **6**, 418–443 (2022).
29. Park M, Verma S, LaPotin A et al. High-emissivity, thermally robust emitters for high power density thermophotovoltaics. *Joule* **9**, 102005 (2025).
30. Rafalskyi D, Martínez JM, Habl L et al. In-orbit demonstration of an iodine electric propulsion system. *Nature* **599**, 411–415 (2021).
31. Lev D, Myers RM, Lemmer KM et al. The technological and commercial expansion of electric propulsion. *Acta Astronaut* **159**, 213–227 (2019).
32. Correia SFH, Bastos ARN, Fu LS et al. Lanthanide-based downshifting layers tested in a solar car race. *Opto-Electron Adv* **2**, 190006 (2019).

## Acknowledgements

K.C. appreciates Prof. Gang Chen from MIT for constructive discussions on TPV device efficiency measurement. This work is sponsored by National Natural Science Foundation of China (52371139), Fundamental and Interdisciplinary Disciplines Breakthrough Plan of the Ministry of Education of China (JYB2025XDXM411), Consulting Decision-Making Project (JCZXSJB2024-07) and SJTU 2030 Initiative. This research made use of shared facilities of Zhiyuan Innovative Research Center (ZIRC) at SJTU, Materials Experimental Education Center (MEEC), Center for Advanced Electronic Materials and Devices (AEMD) and Instrumental Analysis Center (IAC) at SJTU.

## Competing interests

The authors declare no competing financial interests.

## Supplementary information

Supplementary information for this paper is available at
https://doi.org/10.29026/oea.2026.250248

**Open Access** This article is licensed under a Creative Commons Attribution 4.0 International License, which permits use, sharing, adaptation, distribution and reproduction in any medium or format, as long as you give appropriate credit to the original author(s) and the source, provide a link to the Creative Commons license, and indicate if changes were made. To view a copy of this license, visit http://creativecommons.org/licenses/by/4.0/
©The Author(s) 2026.
Published by Editorial Office of *Opto-Electronic Advance*, Institute of Optics and Electronics, Chinese Academy of Sciences.

Opto-Electronic Journals Group
www.oejournal.org
Scan for Article PDF